PHYSICAL REVIEW C VOLUME 51, NUMBER 5 MAY 1995

# $^{16}$O$(\gamma, n)$ reaction at intermediate energy

B-E. Andersson, J-O. Adler, S. A. Bulychjev,* L. Isaksson, H. Ruijter, and B. Schrøder
*Institute of Physics, University of Lund, Sölvegatan 14, S-223 62 Lund, Sweden*

J. R. M. Annand, G. I. Crawford, P. D. Harty, J. C. McGeorge, and G. J. Miller
*Department of Physics and Astronomy, University of Glasgow, G12 8QQ, Scotland*

J. Ryckebusch
*Institute for Nuclear Physics, Proeftuinstraat 86, B-9000 Gent, Belgium*

(Received 1 February 1995)

Measurements of the reaction $^{16}$O$(\gamma, n)$, made with tagged photons at $E_\gamma \sim 58$ MeV, are presented. Neutron energy determination was by time of flight, giving a resolution of $\sim 2$ MeV which enabled the ground-state excitation in $^{15}$O to be resolved from states at 5.2 and 6.2 MeV. Differential cross sections were measured in the angular range 30°–110° and are compared with the predictions of a microscopic, self-consistent Hartree-Fock, random phase approximation model of $(\gamma, N)$ reactions. The implications for the theoretical description are discussed, notably the dependence of the $(\gamma, n)$ cross section on meson exchange currents and final-state rescattering.

PACS number(s): 25.20.Lj, 21.60.Jz, 27.20.+n

## I. INTRODUCTION

At intermediate energy $(\gamma, N)$ reactions provide a relatively clean and potentially illuminating probe of nuclear structure. Initial-state interactions are negligible and, at least for light nuclei, modifications due to final-state interactions (FSI) should not obscure unduly the effects which arise from the coupling of the photon to the various nuclear currents. Broadly speaking at these energies, which fall between the excitation of collective nuclear resonances and nucleon isobar resonances, the photon interacts in one of two ways.

(1) With a one-body current, in which case the internal motion of the nucleon must take up the large mismatch in momentum between the incoming photon and the outgoing nucleon, so that here the photon would probe high-momentum components of the single-particle wave function.

(2) With two-body currents. Absorption on a correlated $p$-$n$ pair obviates the need for a high initial-state momentum, if the nucleons are ejected roughly back to back. Indeed the $(\gamma, pn)$ channel is generally dominant at intermediate energy, but the quasideuteron process also feeds the $(\gamma, N)$ channels when one nucleon is reabsorbed. At the present energies the coupling to one-pion-exchange currents would be expected to be the dominant component of two-nucleon absorption.

In the past decade significant progress has been made both in the experimental techniques for measurement of $(\gamma, N)$ reactions and in the theoretical interpretation of the results.

Early measurements used a bremsstrahlung beam [1,2] and in general only the $(\gamma, N_0)$ transition could reliably be measured from the end-point region of the continuum energy spectrum, the sole part which is unambiguously due to the ground-state transition. $^{16}$O was suitable in this respect as the energy gap from the ground to first excited state is $\sim 5$ MeV in $A = 15$ nuclei, but even here background subtraction requires extreme care. Absolute determination of the photon flux was also difficult and indeed has been cited [3] as a major cause of discrepancies in early measurements of $^2$H$(\gamma, p)$. These difficulties are avoided if a tagged bremsstrahlung beam is used, as both photon energy and flux can be accurately determined. Given the availability of continuous-wave electron accelerators, this technique is now standard in photonuclear physics and, with high quality nucleon spectrometers, discrete excited states of the residual nucleus can be resolved. Where these differ in structure one has the potential to gain additional information. For example, a quasifree-knockout mechanism will exclusively populate simple hole (1h) states, whereas a two-body mechanism will also populate more complex states, when one nucleon is reabsorbed into an unoccupied orbital below the particle emission threshold. At the moment a substantial quantity of tagged-photon data exists for $^{12}$C$(\gamma, N)$ [4–8] and to a lesser extent for $^{40}$Ca$(\gamma, N)$ [9,10]. In the former the highly deformed shape complicates matters and the structure of the $A = 11$ states is somewhat uncertain, while for the latter the density of states in the $A = 39$ system is high so that only $^{40}$Ca$(\gamma, p_0)$ has been resolved. In addition, FSI are expected to play a more important role in the heavier nucleus. $^{16}$O with a simple, well-understood structure which facilitates theoretical calculations, probably represents a better target for study and experimentally offers the opportunity to resolve the $\frac{1}{2}^-$ (ground) and $\frac{3}{2}^-$ (6.2 MeV) states, which have substantial 1h components, from the $\frac{1}{2}^+, \frac{5}{2}^+$ dou-

---

*Present address: ITEP, Moscow 117259, Russia.

0556-2813/95/51(5)/2553(9)/$06.00

blet at $\sim$ 5.2 MeV which is largely two-hole–one-particle (2h1p) in character. However, the bulk of the existing data have been taken with bremsstrahlung [1,2,11].

The $^{16}O(\gamma, p_0)$ cross section has been observed to scale [2] with missing momentum $p_m = p - q$, where $p$ is the ejected nucleon momentum and $q$ the momentum transfer, and was reproduced tolerably well for $E_\gamma < 100$ MeV by a distorted-wave-impulse-approximation (DWIA) calculation [12] similar to those which have proved successful in the analysis of $(e, e'p)$ data. However, a subsequent attempt [13] to treat $(\gamma, p)$ and $(e, e'p)$ in a consistent manner significantly underpredicted the $(\gamma, p)$ cross section. Virtual photon data have mainly been taken in a low $p_m$, parallel kinematics regime, in contrast to $(\gamma, p)$ where the transverse real photon has a much higher $p_m$ and while quasielastic $(e, e'p)$ predominantly populates 1h states, $(\gamma, p)$ also strongly populates states which have large 2h1p components [4]. Further, more telling evidence of the inadequacy of a standard DWIA approach has come from the observation that $\sigma_{\gamma, n_0} \sim \sigma_{\gamma, p_0}$ [1], recently confirmed in a $^{12}C(\gamma, n)$ experiment [7] which shows that the approximate equality holds, irrespective of the structure of the residual states. In any reasonable DWIA calculation [14] $\sigma_{\gamma,n} \ll \sigma_{\gamma,p}$ and an alternative explanation based on the modified quasideuteron model was proposed [15]. Here the photon is assumed to interact with a correlated $p$-$n$ pair, with reabsorption of one of the ejected nucleons. The factorization of terms relating to the photon-pair interaction and the pair-momentum distribution simplifies the calculation. Unsurprisingly the model works quite well, as the shape of the cross section is largely determined by the pair-momentum distribution, with the two-body effects being input phenomenologically via the measured $^2H(\gamma, p)$ cross section. A more microscopic approach [16], which evaluates meson exchange current (MEC) effects through the use of Siegert's theorem, gives a reasonable description of $(\gamma, p)$ while more recent unfactorized theories, which use effective $N$-$N$ interactions and the random phase approximation (RPA) to generate the many-body wave function, have been applied to $(\gamma, N)$ with some success [17,18]. RPA accounts for long-range, final-state $N$-$N$ correlations while two-body current effects result from momentum-dependent-force terms in the Skyrme effective $N$-$N$ interaction. Alternatively DWIA calculations have been extended [19] to include short-range, initial-state $N$-$N$ correlations and a two-body current operator which accounts for MEC. Finally, although the bulk of the microscopic calculations are applicable only to 1h states, an attempt has been made to model transitions to 2h1p states [20] where MEC effects were considered to be fully responsible for the observed strength. Comparison was made with $^{12}C(\gamma, p)$ [20] and $^{12}C(\gamma, n)$ [7] measurements, with agreement being good in the former case, but poor in the latter case.

Thus the theoretical work of the past decade has certainly advanced our understanding of $(\gamma, N)$ processes so that a consistent description of these reactions and $(e, e'N)$ is gradually emerging. However, due to technical difficulty, there is still a lack of high quality $(\gamma, n)$ [and $(e, e'n)$] data which can quantitatively test theoretical predictions and here we present $^{16}O(\gamma, n)$ reaction cross-section results which complement a recent, analagous measurement of $^{16}O(\gamma, p)$ [21]. In the following sections we describe the experimental setup, outline the method of data analysis, and present the measured differential cross sections. These are compared with self-consistent, Hartree-Fock random-phase-approximation (HF-RPA) model calculations and a DWIA calculation which accounts for short-range correlation and MEC effects.

## II. EXPERIMENTAL DETAILS

The experiment was performed at the Lund MAXlab tagged photon facility [22] where a racetrack microtron, pulsed at 50 Hz, injected 75 MeV electrons into a stretcher ring. The extracted beam had a duty cycle of $\sim$ 60% and was fed to the nuclear physics area depicted in Fig. 1. An inclined pole face, magnetic spectrometer tagged the bremsstrahlung produced in a 50 $\mu$m Al radiator and bent the primary electron beam into a shielded, borated-water dump. The bremsstrahlung cone was confined to a half angle of 0.35° by a tapered tungsten-alloy collimator, followed by a sweeping magnet and lead post-collimator. An array of 22 plastic scintillators acted as the spectrometer's focal-plane detector, tagging photons

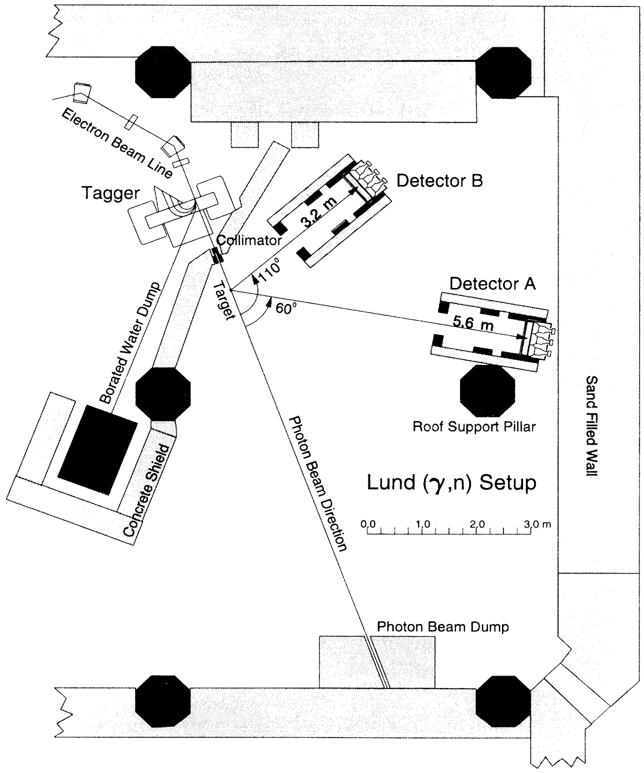

FIG. 1. A plan view of the photonuclear experimental area at MAXlab. The energy resolution of the 110°, 3.2 m flight path detector was $\sim$ 2 MeV, while that of the 60°, 5.6 m detector was $\sim$ 1 MeV.

in the range 55–61 MeV with a resolution of $\sim 0.35$ MeV, determined by the width of the individual scintillators.

Tagging efficiency, the ratio of the number of tagged photons passing through the collimator to the number of electrons detected in the focal plane, was measured using a photon detector with 100% detection efficiency, which consisted of plastic-scintillator fibers embedded in a lead matrix [23]. For the $(\gamma, n)$ experiments the accelerator was run at a current of $\sim$ 15 nA, which produced a summed rate in the focal-plane counters of $\sim 3 \times 10^6$ Hz. However, the resultant bremsstrahlung flux would have overloaded any 100% efficient counter placed in the direct photon beam and so for tagging efficiency measurements the electron current was reduced by a factor of $10^3$. Absolute measurements were made at the start and finish of every $(\gamma, n)$ run, but in the intervening period the relative tagging efficiency was continuously monitored at full beam intensity by a stack of three, 0.5 mm thick plastic scintillators, whose detection efficiency was calibrated against the 100% efficient counter.

The target consisted of distilled water held in a cylindrical aluminum cell of dimensions 90 mm × 50 mm diameter. Entrance and exit foils had a thickness of 0.25 mm which was negligible in comparison to the water. Runs were made with $H_2O$, empty cell for background subtraction and $D_2O$ for checking the absolute cross-section normalization (Sec. III B). The targets were placed with their axes centered on the photon beam axis and aligned parallel to it. At the target position the photon beam diameter, measured using Polaroid film placed behind a metal foil converter, was around 30 mm, comfortably within the confines of the target.

Reaction products from the target were detected in two liquid scintillation counters [24]. Briefly, each consists of a $600 \times 600 \times 100$ mm aluminum tank containing NE213A liquid scintillator, which has a higher flash point than the otherwise very similar NE213. Internal thin partitions subdivide the tank into nine, 200 × 200 × 100 mm cells, each of which has a large-area glass window coupled to a 130 mm photomultiplier via a Lucite light guide. The liquid-scintillator tanks are enclosed except on the rear, photomultiplier side by a "box" consisting of 20 mm thick sheets of NE110 plastic scintillator. This serves to veto charged particles, for example, electrons produced in the target, cosmic rays, and the products of conversion in the shielding which encloses the neutron counters. Light signals from the veto counters are collected in type-NE172 fluorescent light guides before being supplied to 50 mm photomultipliers. NE172 is similar to BBQ, but fluoresces at a shorter wavelength and has a shorter decay constant which allows higher counting rates. Background neutrons and photons are attenuated by blocks of borated wax and lead, which are built around the aluminum tank and extended toward the target so that the detector directly sees only the immediate target area. The entire assembly sits on an iron table supported by air pads which facilitate movement.

Neutron energy determination was by time of flight (TOF), measured with respect to a hit on the tagger focal plane. The signal from each focal-plane scintillator was fed to a constant-fraction discriminator (CFD) whose logic output was delayed and then fed to the stop of a time-to-digital converter (TDC). TDC starts were provided by the logical OR of the 16 signals from the neutron detector elements (two elements of one detector were not operational), again after time pick-off in CFD's, and the TDC conversion gain was determined using a proprietary, crystal-oscillator-driven calibrator.

The time zero points on TDC spectra were extrapolated from a measurement of relativistic electrons produced in the target by tagged bremsstrahlung. For this the forward veto plastic scintillator was in coincidence (as opposed to anticoincidence for normal running) with the liquid scintillator. These measurements, which were made whenever the detectors were moved, produced a well-defined peak (Fig. 2) in the focal-plane-detector TDC spectra and therefore additionally gave a measurement of the intrinsic timing resolution of the system. The resolution of 0.8 ns full width at half maximum (FWHM) contains small components from uncertainties in target interaction position and overall flight path, but is mainly due to the time-pick-off jitter of analog signals feeding into CFD's. At the maximum neutron kinetic energies encountered in the present experiment, $\sim$ 40 MeV, the flight-time uncertainty across the 100 mm thickness of liquid scintillator is $\sim$ 1.2 ns, which produces an overall uncertainty in detection time of $\sim$ 1.4 ns. Except at $\theta_n = 60^\circ$ flight paths ranged from 2.5 to 3.5 m which gave neutron energy resolutions of 2.0 – 2.5 MeV FWHM, sufficient to resolve $(\gamma, n_0)$ cleanly from reactions leading to more highly excited residual states. Separation of the positive-parity doublet at 5.2 MeV from the $\frac{3}{2}^-$ state at 6.2 MeV in $^{15}$O requires a resolution of $\sim$ 1 MeV FWHM and was achieved at $\theta_n = 60^\circ$ where the flight path was 5.6 m.

Calibration of the liquid-scintillator pulse height has no bearing on neutron energy determination, but is important for neutron detection efficiency evaluation. Thus the pulse-height distributions from the gamma-ray lines of $^{228}$Th(2.6 MeV) and $^{241}$Am – Be(4.4, 6.1 MeV) were recorded and the well-defined Compton edges used to provide calibration points for the neutron detection thresholds.

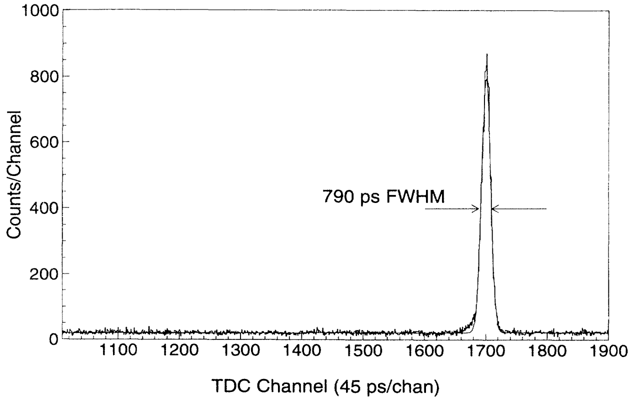

FIG. 2. A time-zero spectrum, showing the prominant peak associated with the detection of tagged-photon-induced Compton and pair electrons.

As outlined above, it is relatively easy to distinguish charged from neutral particles in the TOF spectrometer. However, in experiments of this type the number of photons detected is likely to be several orders of magnitude greater than the number of neutrons, necessitating further discrimination. The effective decay time of the liquid-scintillator signal depends on the velocity of the recoil charged particle, so that pulse-shape discrimination (PSD) may be used to distinguish neutrons from photons. An electronic module, designed at the University of Glasgow [25], was used for this purpose and gave clean separation of recoil protons from recoil electrons (Fig. 3). A logic signal, produced on the detection of an electron, inhibited the registration of a particular event, so that the bulk of events where a photon was detected were discarded on-line.

Each focal-plane detector was equipped with a TDC to record TOF information and each neutron detector had an associated charge-to-digital convertor (QDC) to register its pulse amplitude as well as a TDC, to determine which element had fired and register any time correlations between the neutron detector cells. Additionally the pulse shape, analog outputs from the 16 PSD modules were stored in separate QDC's to record the $n/\gamma$ discrimination threshold. Digitized signals from the detector system were read via CAMAC to a VMEbus microcomputer which stored these data event-by-event on magnetic tape.

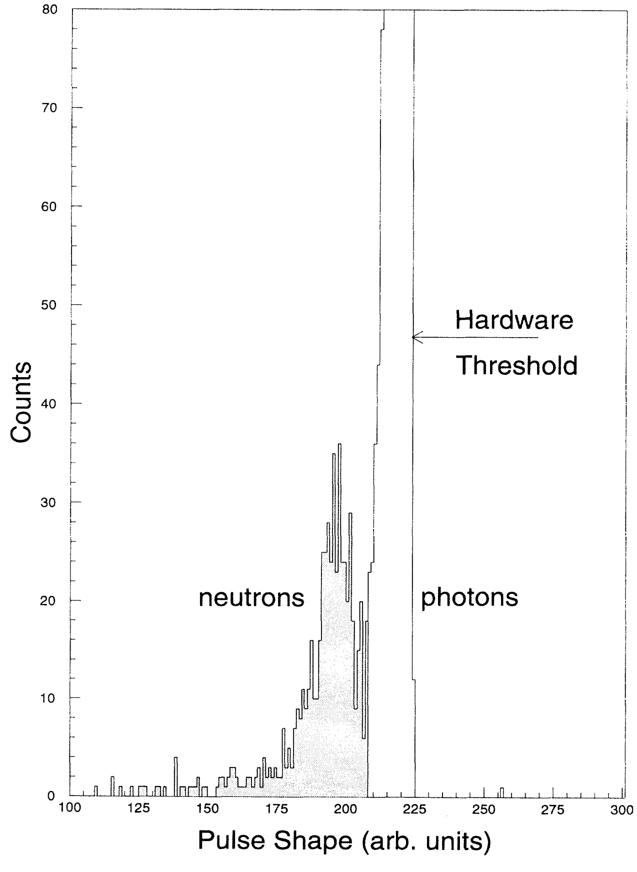

FIG. 3. The separation of neutrons (recoil protons) from photons (recoil electrons) by the pulse-shape analysis method. The shaded area indicates the software cut made on protons.

## III. DATA REDUCTION AND ANALYSIS

The data produced by the detector system were monitored on-line to check for any malfunction. Off-line replays of the data tapes were then used to make careful calibrations of the system, which allowed a more precise selection of events of interest than was possible on-line.

### A. Method of analysis

The PSD modules were deliberately adjusted (Fig. 3) to allow some detected-photon events into the data, to ensure that no neutrons were lost and to aid the evaluation of random-coincidence background (see below). However, by defining windows of interest on plots of pulse shape these events were filtered out and only detected-neutron events were analyzed. Using the calibrations of time-zero TDC channel and TDC conversion gain (Sec. II) neutron flight times were determined. These gave neutron kinetic energies, which together with the known $E_\gamma$ and $\theta_n$, were used to calculate the excitation energy of the residual nucleus, $E_x = E_\gamma - T_n - T_{A-1} + Q$, event by event. Values of $E_x$ relating to the individual elements of a neutron detector and individual tagger focal-plane counters were obtained and then sorted into a common spectrum, which was thus averaged over the tagged energy range (55–61 MeV) and the angle subtended by a liquid-scintillator array (6–7°).

A sample spectrum of $E_x$ evaluated in this manner is given in Fig. 4, from which it is evident that structure associated with excitation of low-lying states in $^{15}$O sits on top of a substantial background. The contents of the spectrum arise from three sources: (1) neutron counts produced in the water target by tagged photons, (2) neutron counts produced in the water target by untagged photons, and (3) neutron counts produced in the target cell walls by tagged and untagged photons and additionally neutrons which are produced outside of the target area, e.g., from the electron or photon beam dumps (Fig. 1).

The counts of interest (source 1) are therefore given by

$$C_1 = C_{1+2+3} - k_2 C_2 - k_3 C_3$$

where $C_{1+2+3}$ is the combined number of counts from sources 1, 2, and 3, and so on, $k_2$ is the random background normalization coefficient and $k_3$ was determined from the measured photon flux difference for full and empty-target experimental runs. The effective thickness of target cell walls and air in the vicinity of the target was negligible in comparison to the 9 g/cm$^2$ of the target itself and no significant counting rate from neutrons produced outside of the target region was observed. Thus empty-cell corrections were very small and there remained the problem of evaluating the random coincidences from source 2. Since we tagged only a 55–61 MeV bite of the 25–75 MeV bremsstrahlung continuum which produced detectable neutrons, the ratio of tagged to untagged photo-neutrons was small and the rate of random coincidences relatively high, even at the fairly low beam intensity used in the present experiment. The spectrum of $C_2$ was estimated by selecting events where a photon was detected (Fig. 3) in the liquid scintillator and using these to generate a spectrum of $E_x$, as for neutrons. As detected particles are emitted predominantly from the target the photon "TOF" spectrum has a single prompt coincidence peak, similar to Fig. 2 but less prominant, which sits on a structureless, almost flat random background. The peak is well separated from any real neutron TOF signal and thus the background should mimic the shape of the random-neutron-produced distribution. It should be noted that on conversion from TDC channel to $E_x$ space the shape of the random distribution changes, rising with increasing $E_x$, which results from the approximate $1/t^2$ dependence of the neutron kinetic energy. The normalization coefficient $k_2$ was determined by setting

$$\left[\frac{\sum C_{1+2}}{k_2\sum C_2}\right]^{E_x<0}\left[\frac{\sum C_{1+2}}{k_2\sum C_2}\right]^{E_x>E_{\max}}=1,$$

where $E_{\max}$ is the maximum excitation that neutrons could produce, which depends on photon energy and neutron detection threshold. The threshold, set in hardware by the liquid-scintillator CFD's, corresponded to 4 MeVee (MeV electron equivalent), but a range of higher values were imposed by software cuts on the pulse-height spectra, to investigate if the random background subtraction could be optimized. Most of the random neutrons have lower kinetic energy than the prompt ones since the photoemission cross section rises rapidly with decreasing $E_\gamma$ and thus their detection efficiency is preferentially reduced by raising the threshold. Optimum statistical uncertainty was achieved with a threshold value of $\sim$ 7 MeVee.

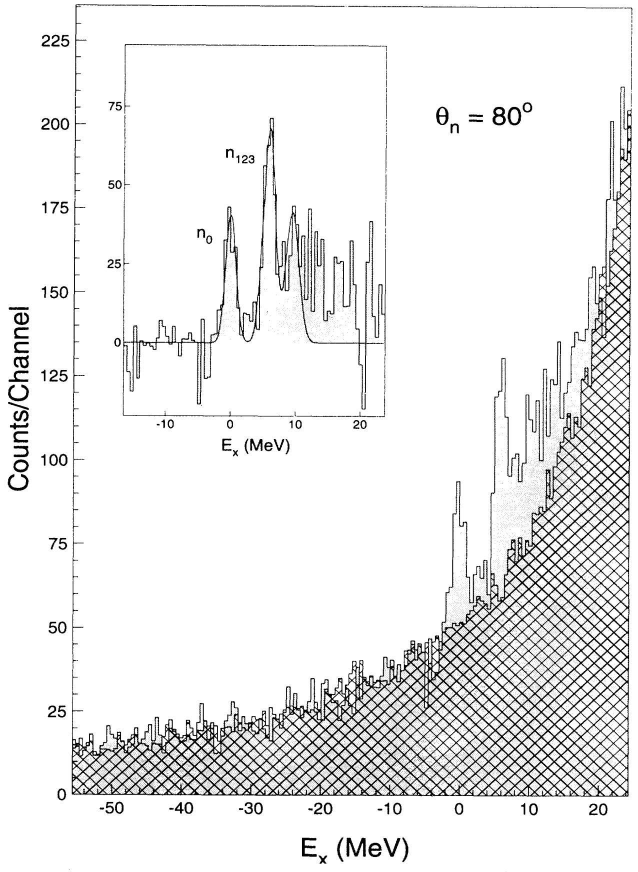

FIG. 4. An excitation energy spectrum of $^{15}$O produced by $^{16}$O($\gamma,n$). The cross-hatched, normalized random background spectrum is subtracted from the shaded spectrum which contains prompt and random contributions to produce the spectrum shown in the inset.

After random subtraction the excitation energy spectrum (inset Fig. 4) exhibits a flat, zero background for $E_x < 0$, followed by peaks which result from excitation of low-lying states in $^{15}$O. At higher excitation, where counts steadily decrease due to the falling detection efficiency, unresolved states in $^{15}$O are superimposed on the continuum from the $^{16}$O($\gamma,pn$) reaction. Gaussian fits were made to determine the number of counts in the observed peaks, where the positions were constrained by the knowledge of the $^{15}$O excitation energies and shapes determined from the well-resolved ($\gamma,n_0$) distribution, taking account of the improvement in resolution with increasing $E_x$. Apart from the measurement at $\theta_n = 60°$, the excitations in the range 5.18 – 6.18 MeV, which were fitted with two separate Gaussians, were not resolved and their areas were combined before comparison with theory. Contamination of the 6.18 state by the tails of higher unresolved excitations was modeled by simultaneously fitting a further two Gaussians, centered at 7.0 and 9.0 MeV and resulted in an additional uncertainty in areas of the peaks at 5.18 and 6.18 MeV.

### B. Absolute cross-section determination and systematic uncertainties

The differential cross section is given by

$$\sigma(\theta)=\frac{N_n}{N_a N_e \Omega_n \epsilon_t \epsilon_l \epsilon_n \eta},$$

where the parameters are as follows: $N_n$ is the integrated area of a peak; $N_a$ is the effective number of atoms in the target, calculated using an effective target length which accounts for photon attenuation in the target; $N_e$ is the number of electrons detected in the tagger focal plane; $\Omega_n$ is the solid angle subtended by a neutron detector, evaluated using a straightforward Monte Carlo procedure; $\epsilon_t$ is the measured tagging efficiency (Sec. II); $\epsilon_l$ is the fractional live time of the data acquisition system, measured by gating a pulser of known frequency with the "acquisition-system-live" output and recording the subsequent counting rate in a scaler; $\epsilon_n$ is the kinetic-energy-dependent neutron detection efficiency calculated using the Monte Carlo code STANTON [26]; $\eta$ is the neutron transmission of the target, evaluated in a Monte Carlo procedure using $n$+$^{16}$O and $n+p$ reaction cross sections.

The systematic uncertainties associated with each parameter are given in Table I and when added in quadra-

TABLE I. Percentage systematic uncertainties in the quantities used to calculate the differential cross section.

| Parameter | $\frac{\delta N_n}{N_n}$ | $\frac{\delta N_a}{N_a}$ | $\frac{\delta N_e}{N_e}$ | $\frac{\delta \Omega_n}{\Omega_n}$ | $\frac{\delta \epsilon_t}{\epsilon_t}$ | $\frac{\delta \epsilon_l}{\epsilon_l}$ | $\frac{\delta \epsilon_n}{\epsilon_n}$ | $\frac{\delta \eta}{\eta}$ |
|---|---|---|---|---|---|---|---|---|
| Min value | 4.3 | 0.5 | 2.2 | 0.2 | 2.3 | 3.0 | 10.0 | 5.0 |
| Max value | 10.3 | 2.9 | 2.2 | 0.4 | 2.3 | 10.0 | 10.0 | 5.0 |

ture give a total systematic uncertainty, which varies from 12.5 to 15 %. A large contribution is the uncertainty in the detection efficiency, the value of 10% being estimated on the basis of comparisons of STANTON [26] results with previous measurements and on the spread of values obtained when these calculations were compared with the predictions of other codes [27]. As this was a somewhat qualitative procedure we sought other means to check the cross-section normalization.

The two-body photodisintegration cross section of deuterium is probably the most widely measured quantity in photonuclear physics and, on the basis of recent parametrizations of the available data [28,29], is now known to ~5% uncertainty over a wide range of energies. We have therefore measured the $^2H(\gamma,n)$ differential cross section at the same energies and laboratory angles as in the $^{16}O(\gamma,n)$ experiment using a $D_2O$ target. Spectra of $E_x$ were generated for $D_2O$ and $H_2O$ target runs assuming $^2H(\gamma,n)$ reaction kinematics and subtraction of the $H_2O$ from $D_2O$ data yielded an unambiguous signal, which was integrated and used to calculate $\sigma(\theta)$ in the manner outlined above. The measured photodisintegration differential cross section, converted to equivalent proton c.m. angle, is compared with the curves calculated from the parametrizations of Refs. [28,29] in Fig. 5. It is evident that the data overlap the curves, showing that the systematic uncertainties quoted in Table I are not underestimated.

## IV. RESULTS AND THEORETICAL COMPARISONS

The measured differential cross sections are displayed in Fig. 6 for $(\gamma,n_0)$, which is well resolved (Fig. 4), and $(\gamma,n_{1,2,3})$, which contains contributions from unresolved $\frac{1}{2}^+$, $\frac{5}{2}^+$, and $\frac{3}{2}^-$ excitations. We compare the present $n_0$ data [Fig. 6(a)] with those of Ref. [1] measured in Mainz using bremsstrahlung, and Ref. [30] measured recently

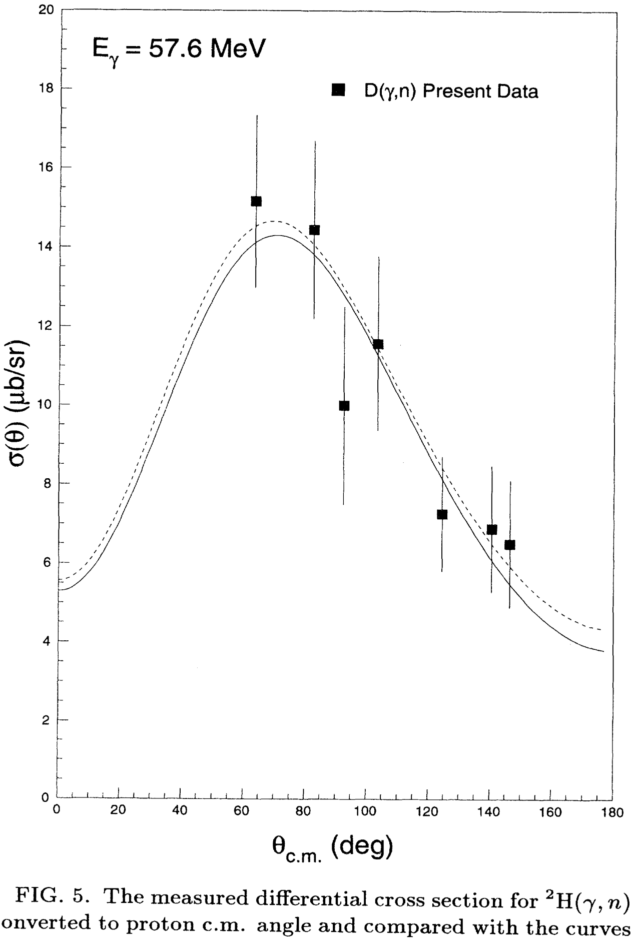

FIG. 5. The measured differential cross section for $^2H(\gamma,n)$ converted to proton c.m. angle and compared with the curves produced by the parametrizations of Jenkins *et al.* (solid line) and Rossi *et al.* (dotted line). Error bars display the combination of statistical and systematic uncertainties.

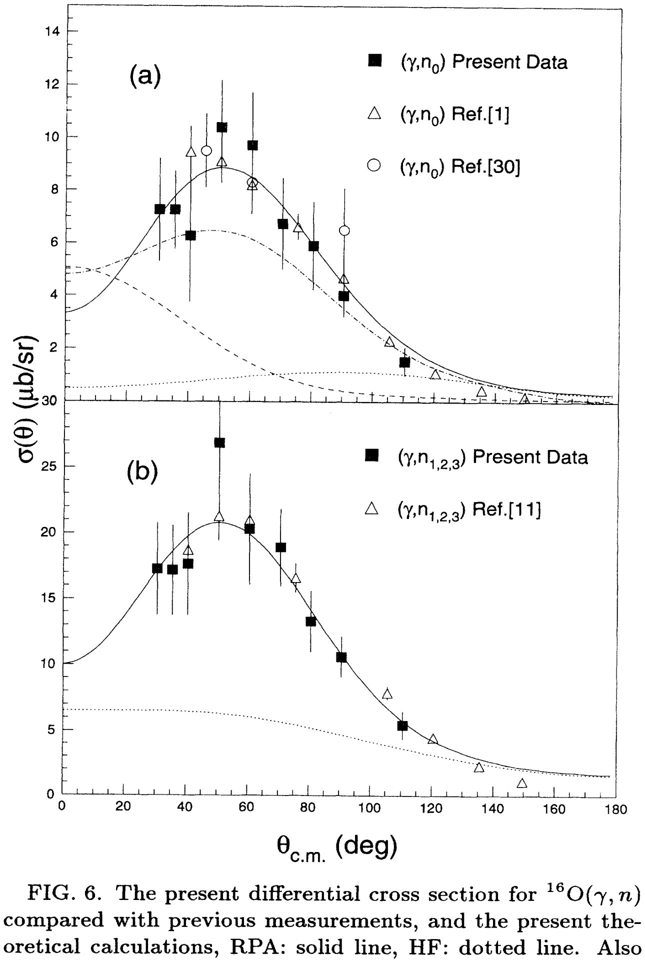

FIG. 6. The present differential cross section for $^{16}O(\gamma,n)$ compared with previous measurements, and the present theoretical calculations, RPA: solid line, HF: dotted line. Also shown are the predictions of Benenti *et al.*, two-body-current operator: dot-dashed line, one-body including short-range correlations: dashed line. Error bars as in Fig. 5.

with tagged photons. Agreement between the data sets is good, but the present measurement extends further forward in angle and exhibits a peak at $\theta_n \sim 50°$, reminiscent of the shape observed in $^{12}$C$(\gamma, n_0)$ [7] at similar energy. For the $(\gamma, n_{1,2,3})$ results [Fig. 6(b)] there are no significant differences between the present data and those of Ref. [11] and again the differential cross section is observed to peak at $\theta_n \sim 50°$. In Fig. 7 the present $(\gamma, n)$ differential cross sections are compared with recent $^{16}$O$(\gamma, p)$ measurements [21] where the $p_{1,2}$ doublet was resolved from $p_3$. Apart from the measurement at 60° this was not the case for $(\gamma, n)$ and so for the purposes of comparison the $(\gamma, n_{1,2})$ cross section was estimated at $\theta_n \neq 60°$ from the theoretical calculations described below and subtracted from the $(\gamma, n_{1,2,3})$ data, to produce the $(\gamma, n_3)^*$ angular distribution in Fig. 7(b). Again the general observation that $\sigma_{\gamma,n} \sim \sigma_{\gamma,p}$ is upheld, although systematic differences do appear, especially in $(\gamma, N_0)$ [Fig. 7(a)] where $\sigma_{\gamma,p}(\theta)$ peaks at more forward angles where it has a larger magnitude. A similar, if less clear cut, effect is visible in $(\gamma, N_3)$. The single $(\gamma, n_{1,2})$ data point, compared in Fig. 7(c) to the $(\gamma, p_{1,2})$ data of Ref. [21], shows no statistically significant difference and clearly a full angular distribution would be desirable.

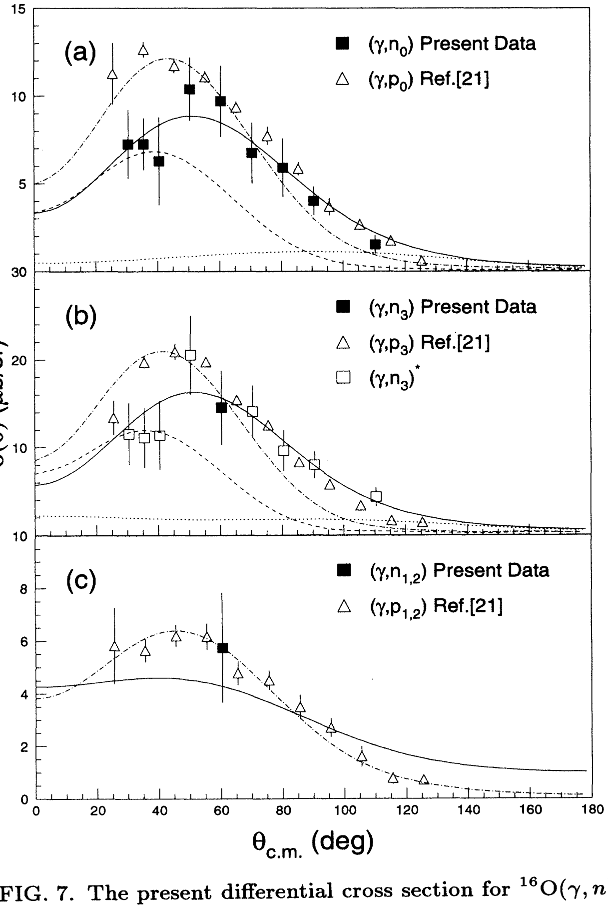

FIG. 7. The present differential cross section for $^{16}$O$(\gamma, n)$ compared with equivalent $(\gamma, p)$ data. The solid and dot-dashed curves denote the HF-RPA calculations for $(\gamma, n)$ and $(\gamma, p)$, respectively. The dotted and dashed curves denote the HF calculations for $(\gamma, n)$ and $(\gamma, p)$, respectively. Error bars as in Fig. 5.

The data of Figs. 6 and 7 are compared with the results of a coupled-channels calculation which was performed within a continuum HF-RPA framework, all channel couplings between single-proton and neutron knockout from the $1s_{1/2}$, $1p_{3/2}$, and $1p_{1/2}$ orbitals being implemented. Consequently, $(\gamma, n_0)$, $(\gamma, n_3)$, $(\gamma, p_0)$, and $(\gamma, p_3)$ differential cross sections were obtained within a consistent framework. As the $\frac{1}{2}^-$ and $\frac{3}{2}^-$ states were assumed to be pure 1h, the calculations have been multiplied by spectroscopic factors, extracted from an equivalent analysis [31] of $^{16}$O$(e, e'p)$ data. In the description of the initial photoabsorption mechanism the current operator, obtained by minimal substitution in the Hamiltonian [32], includes both one-body and two-body terms. The latter was essentially determined by the momentum-dependent-force component of the extended Skyrme-type effective $N$-$N$ interaction used for the present coupled-channels calculations, so that the two-body absorption mechanism and channel couplings are treated in a consistent manner. Further we wish to stress that the estimation of two-body-current effects does not rely on Siegert's theorem. To assess the importance of final-state rescattering, equivalent direct-knockout calculations, labeled HF in Figs. 6 and 7, were made using the same Skyrme interaction. Thus although these include the effect of two-body photoabsorption they produce rather different results for $(\gamma, n)$ and $(\gamma, p)$. The former is far below the data, while the latter, in which quasifree knockout is significant, is a factor $\sim$ 2 low. Only after the inclusion of coupling with other one-nucleon-emission channels is good agreement with the data achieved, supporting the idea [16] that giant resonance influences persist into the intermediate energy region. However this multistep rescattering, which is not implemented in an optical potential description of FSI, has a much more pronounced effect in $(\gamma, n)$ than in the equivalent $(\gamma, p)$ channels.

The other calculations shown in Fig. 6(a) [19] use an extension of the Pavia DWIA approach. Here the many-body nuclear wave function contains correlation terms of the Jastrow type and the current operator has a two-body part, derived from the one-pion-exchange potential, where only the seagull term has been retained. Of the neglected contributions the pion-in-flight term, which strictly speaking is necessary to preserve charge-current conservation, has been shown to interfere strongly and destructively with the seagull term [33], leading to a considerable reduction of the predicted MEC effect. The calculation gives a fair description of the $(\gamma, n_0)$ cross section, and predicts a dominant MEC effect in that the angle integrated cross section rises from 13 to 44 $\mu$b when the two-body-current operator is switched on. However, it should be noted that initial- and final-state wave functions are not orthogonal and in addition that the optical potential [34], used to simulate FSI, is not the best available. Indeed the calculation is highly sensitive to this parameter with the integrated cross section dropping from 44 $\mu$b to 12.6 $\mu$b if the potential of Ref. [35] is chosen.

The differential cross sections for the $(\gamma, N_{1,2})$ doublet [Fig. 7(c)] cannot be obtained in a coupled-channels calculation of the RPA type as the predominant underlying structure of the $\frac{5}{2}^{+}$ and $\frac{1}{2}^{+}$ states is not 1h. Spectroscopic factors, which are ~2% of the sum-rule value [36], were determined for the $1d_{5/2}$ ($\frac{5}{2}^{+}$) and $2s_{1/2}$ ($\frac{1}{2}^{+}$) components in an analysis of high resolution $^{16}$O$(e,e'p)$ data, but each state has a much larger 2h1p component which can be excited in a direct-knockout mechanism after photoabsorption on two-body currents. The dominant 2h1p components for the doublet states are $|(1p_{1/2})^{-2}(1d_{5/2})\rangle$ ($\frac{5}{2}^{+}$) and $|(1p_{1/2})^{-2}(2s_{1/2})\rangle$ ($\frac{1}{2}^{+}$) and differential cross sections have been calculated in a direct-knockout model, where we consider excitation of both the 1h and 2h1p components in the overlap matrix elements that produce the final cross sections. Here we have used the nonrelativistic reduction of the two-body currents derived from the one-pion-exchange potential, in which seagull and pion-in-flight terms are considered. This two-body current excites both 1h and 2h1p components, whereas one-body photoabsorption uniquely feeds the 1h component. The amplitudes for the 1h and 2h1p components, which are the spectroscopic information entering the calculation, were taken from an equivalent $^{16}$O$(\gamma,p)$ calculation [21] and just as in that case the calculated cross section for the 5.2 MeV doublet is dominated by the $\frac{5}{2}^{+}$ state. As shown in Fig. 7(c) the $(\gamma,n_{1,2})$ data point is consistent with the calculation, which for $(\gamma,n)$ has a less peaked shape than the $(\gamma,p)$ case. In the case of $^{12}$C$(\gamma,N)$ reactions to the triplet of states at $E_x \sim 7$ MeV, which are also largely 2h1p in character, the measured $(\gamma,n)$ [7] and $(\gamma,p)$ [37] differential cross sections are markedly different at forward angles, with the former exhibiting a pronounced peak at $\theta_n \sim 60°$. This is not reproduced in the calculations [20] which were made in a similar manner to that described above for the $A = 15$ doublet, except that the states were assumed pure 2h1p.

## V. SUMMARY AND CONCLUSION

Differential cross sections for the $^{16}$O$(\gamma,n)$ reaction to low-lying states in $^{15}$O have been measured at an average photon energy of 58 MeV and a comparison of these results with recent, analagous $^{16}$O$(\gamma,p)$ data confirms the broad similarity between $(\gamma,n)$ and $(\gamma,p)$ cross sections at intermediate energy. However differences in detail do exist, notably in $(\gamma,N_0)$ at forward angles, and where the mainly 1h $\frac{1}{2}^{-}$ and $\frac{3}{2}^{-}$ states are excited the differential cross sections are rather well reproduced by self-consistent HF-RPA calculations, which in spite of the similarities suggest that the reaction mechanism is somewhat different for $(\gamma,n)$ and $(\gamma,p)$.

In the RPA picture $(\gamma,n)$ strength at $E_\gamma \sim 60$ MeV arises predominantly from final-state rescattering with a relatively minor contribution from MEC [32], whereas in $(\gamma,p)$ quasifree knockout, MEC and final-state rescattering all have significant effects. This is at odds with the results of extended DWIA calculations, which predict a dominant MEC effect in $(\gamma,n)$ and a relatively smaller effect in $(\gamma,p)$ although in both MEC effects might be overestimated due to neglect of the pion-in-flight term. Clearly a more sophisticated treatment of two-body currents is desirable, but a recalculation using a better optical model potential, as employed in modern analyses of $(e,e'p)$ and $(\gamma,p)$ would help to assess the quantitative predictive powers of this model in its present state. To clarify the question of the reaction mechanism in $(\gamma,n)$ more good quality data are required. A range of targets (experiments to measure $^4$He and $^{40}$Ca are under analysis) would further test the magnitude of the effect of final-state rescattering. This would be expected to decrease with increasing energy as coupling to giant resonances becomes less important, possibly producing a clearer signal for MEC or short-range correlation effects. However, the scarcity and lack of precision of the higher energy data currently available testify to the inherent technical difficulty in pursuing such a course of measurements.

In the case of $(\gamma,n_{1,2})$ which populates the $\frac{1}{2}^{+}$, $\frac{5}{2}^{+}$ doublet only one angle was measured, which showed no statistically significant departure from a direct-knockout-model calculation where coupling to one- and two-body currents was considered. For $^{12}$C$(\gamma,N)$ populating the triplet of states at ~ 7 MeV, which are also mainly 2h1p in structure, the $(\gamma,n)$ angular distribution is rather different from $(\gamma,p)$ and it would be of interest to make a similar comparison for $^{16}$O.

## ACKNOWLEDGMENTS

We are indebted to the staff who maintained the smooth running of the MAXlab accelerator and to G. Benenti who provided the results of DWIA model calculations. We acknowledge the support of the Swedish Natural Science Research Council, the Knut and Alice Wallenberg Foundation, the Swedish Institute, the Crafoord Foundation, the U.K. Science and Engineering Research Council, and NATO Grant No. CRG920171.

---

[1] H. Göringer, B. Schoch, and G. Lührs, Nucl. Phys. **A384**, 414 (1982).

[2] D. J. S. Findlay and R. O. Owens, Nucl. Phys. **A292**, 53 (1977).

[3] A. E. Thoraclius and H. W. Fearing, Phys. Rev. C **33**, 1830 (1986).

[4] S. V. Springham, D. Branford, T. Davinson, A. C. Shotter, J. Yorkston, J. C. McGeorge, J. D. Kellie, S. J. Hall, R. Beck, P. Jennewein, and B. Schoch, Nucl. Phys. **A517**, 93 (1990).

[5] L. Van Hoorebeke, D. Ryckbosch, R. Van de Vyver, H. Ferdinande, D. Nilsson, J-O. Adler, B-E. Andersson, K. I. Blomqvist, L. Isaksson, A. Sandell, B. Schrøder, and K. Ziakas, Phys. Rev. C **42**, R1179 (1990).

[6] P. D. Harty, M. N. Thompson, G. J. O'Keefe, R. P. Rasool, K. Mori, Y. Fujii, T. Suda, I. Nomura, O. Konno, T. Terasawa, and Y. Torizuka, Phys. Rev. C **37**, 13 (1988).

[7] J. R. M. Annand, G. I. Crawford, P. D. Harty, J. C. McGeorge, G. J. Miller, B-E. Andersson, J-O. Adler, S. A. Bulychjev, L. Isaksson, H. Ruijter, and B. Schrøder,

Phys. Rev. Lett. **71**, 2703 (1993).

[8] P. D. Harty, J. C. McGeorge, I. J. D. MacGregor, R. O. Owens, J. R. M. Annand, I. Anthony, G. I. Crawford, S. N. Dancer, S. J. Hall, J. D. Kellie, G. J. Miller, B. Schoch, R. Beck, H. Schmieden, J. M. Vogt, and J. Ryckebusch, Phys. Rev. C **51**, 1982 (1995).

[9] C. Van den Abeele, D. Ryckbosch, J. Dias, L. Van Hoorebeke, R. Van de Vyver, J-O. Adler, K. Hansen, L. Isaksson, H. Ruijter, and B. Schrøder, Phys. Rev. C (to be published).

[10] J. A. Eden, G. J. O'Keefe, R. P. Rassool, D. J. McLean, M. N. Thompson, T. Suda, I. Nomura, J. Yokokawa, O. Konno, T. Terasawa, and Y. Torizuka, Phys. Rev. C **44**, 753 (1991).

[11] B. Schoch and H. Göringer, Phys. Lett. **109B**, 11 (1982).

[12] S. Boffi, C. Giusti, and F. D. Pacati, Nucl. Phys. **A358**, 91 (1981).

[13] G. van der Steenhoven and H. P. Blok, Phys. Rev. C **42**, 2597 (1990).

[14] S. Boffi, F. Capuzzi, C. Giusti, and F. D. Pacati, Nucl. Phys. **A436**, 438 (1985).

[15] B. Schoch, Phys. Rev. Lett. **41**, 80 (1978).

[16] M. Gari and H. Hebach, Phys. Rep. **72**, 1 (1981).

[17] M. Cavinato, M. Marangoni, and A. M. Saruis, Nucl. Phys. **A422**, 237 (1984).

[18] J. Ryckebusch, M. Waroquier, K. Heyde, J. Moreau, and D. Ryckbosch, Nucl. Phys. **A476**, 237 (1988).

[19] G. Benenti, C. Giusti, and F. D. Pacati, Nucl. Phys. **A574**, 716 (1994); and (private communication).

[20] J. Ryckebusch, K. Heyde, L. Machenil, D. Ryckbosch, M. Vanderhaeghen, and M. Waroquier, Phys. Rev. C **46**, R829 (1992)

[21] G. J. Miller, J. C. McGeorge, J. R. M. Annand, G. I. Crawford, V. Holliday, I. J. D. MacGregor, R. O. Owens, J. Ryckebusch, J-O. Adler, B-E. Andersson, L. Isaksson, and B. Schrøder, Nucl. Phys. A (in press).

[22] J-O. Adler, B-E. Andersson, K. I. Blomqvist, B. Forkman, K. Hansen, L. Isaksson, K. Lindgren, D. Nilsson, A. Sandell, B. Schrøder, and K. Ziakas, Nucl. Instrum. Methods Phys. A **294**, 15 (1990).

[23] D. W. Hertzog, P. T. Debevec, R. A. Eisenstein, N. A. Graham, S. A. Hughes, P. E. Reimer, and R. L. Taylor, Nucl. Instrum. Methods Phys. A **294**, 446 (1990).

[24] J. R. M. Annand *et al.*, Nuclear Structure Annual Report, University of Glasgow, 1990 [Nucl. Instrum. Methods Phys. A (to be published)].

[25] J. R. M. Annand, Nucl. Instrum. Methods Phys. A **262**, 371 (1987).

[26] R. A. Cecil, B. D. Anderson, and R. Madey, Nucl. Instrum. Methods **161**, 439 (1979).

[27] B-E. Andersson, Ph.D. thesis, University of Lund (1994).

[28] D. A. Jenkins, P. T. Debevec, and P. D. Harty, Phys. Rev. C **50**, 74 (1994).

[29] P. Rossi, E. De Sanctis, P. Levi Sandri, N. Bianchi, C. Guaraldo, V. Lucherini, V. Muccifora, E. Polli, A. R. Reolon, and G. M. Urciuoli, Phys. Rev. C **40**, 2412 (1989).

[30] G. J. O'Keefe, Ph.D. thesis, University of Melbourne (1994).

[31] V. Van der Sluys, J. Ryckebusch, and M. Waroquier, Phys. Rev. C **49**, 2695 (1994).

[32] J. Ryckebusch, Proceedings of the Workshop on Nuclear Physics with Real Photons below Pion Threshold, Laboratorium voor Kernfysica, Rijksuniversiteit, Gent, 19 (1989).

[33] M. VanderHaegen, L. Machenil, J. Ryckebusch, and M. Waroquier, Nucl. Phys. **A580**, 551 (1994).

[34] D. F. Jackson and I. Abdul-Jalil, J. Phys. G **6**, 481 (1980).

[35] A. Nadasen, P. Schwandt, P. P. Singh, A. D. Bacher, P. T. Debevec, W. W. Jacobs, M. D. Kaitchuk, and T. R. Donoghue, Phys. Rev. C **23**, 1 (1981).

[36] M. Leushner, J. R. Calarco, F. W. Hersman, E. Jans, G. J. Kramer, L. Lapikas, G. van der Steenhoven, P. K. A. de Witt Huberts, H. P. Blok, and N. Kalantar-Nayestanaki, Phys. Rev. C **49**, 955 (1994).

[37] H. Ruijter *et al.* (unpublished data).

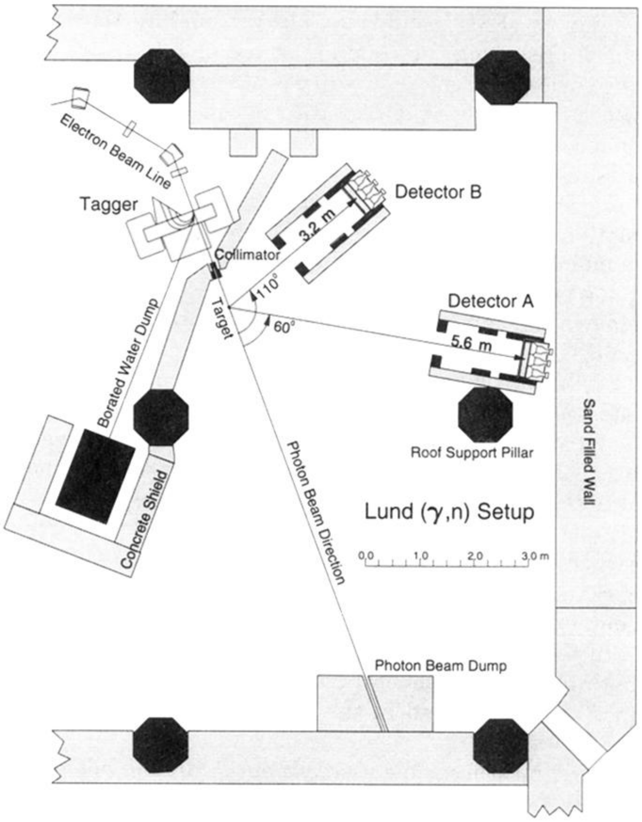

FIG. 1. A plan view of the photonuclear experimental area at MAXlab. The energy resolution of the 110°, 3.2 m flight path detector was ~ 2 MeV, while that of the 60°, 5.6 m detector was ~ 1 MeV.